arXiv:2506.04732v1 [math.NA] 5 Jun 2025

A Fast, Accurate and Oscillation-free Spectral Collocation Solver for High-dimensional Transport Problems

Nicola Cavallini[1], Gianmarco Manzini[2], Daniele Funaro[3,4], and Andrea Favalli[1,2,*]

[1]European Commission, Joint Research Centre, Via Enrico Fermi, Ispra, I -21027 (Va), Italy
[2]Los Alamos National Laboratory, P.O. Box 1663, Los Alamos, NM 87545, USA
[3]Dipartimento di Scienze Chimiche e Geologiche, Università di Modena e Reggio Emilia, Via Campi 103, 41125 Modena, Italy
[4]Istituto di Matematica e Applicata e Tecnologie Informatiche del CNR, via Ferrata 1, 27100 Pavia, Italy
*andrea.favalli@ec.europa.eu

Abstract

Transport phenomena—describing the movement of particles, energy, or other physical quantities—are fundamental in various scientific disciplines, including nuclear physics, plasma physics, astrophysics, engineering, and the natural sciences. However, solving the associated seven-dimensional transport equations poses a significant computational challenge due to the curse of dimensionality. We introduce the Tensor Train Superconsistent Spectral (T^2S^2) solver to address this challenge, integrating Spectral Collocation for exponential convergence, Superconsistency for stabilization in transport-dominated regimes, and Tensor Train format for substantial data compression. T^2S^2 enforces a dimension-wise superconsistent condition compatible with tensor structures, achieving extremely low compression ratios, such as $\mathcal{O}(10^{-12})$, while preserving spectral accuracy. Numerical experiments on linear problems demonstrate that T^2S^2 can solve high-dimensional transport problems in minutes on standard hardware, making previously intractable problems computationally feasible. This advancement opens new avenues for efficiently and accurately modeling complex transport phenomena.

Introduction

Transport phenomena are fundamental across a wide range of scientific disciplines, including nuclear physics, plasma physics, high-energy density physics, astrophysics, condensed matter physics, atmospheric science, oceanography, and engineering. These processes describe the movement and interaction of particles, energy, and other physical quantities within various media. At the heart of modeling these phenomena are transport equations, which comprehensively describe how quantities propagate and interact. For example, the neutron transport equation is fundamental in applications such as reactor design and radiation detection instrumentation, while the Vlasov equation is pivotal in plasma physics, describing the evolution of charged particles under electromagnetic fields, and is fundamental in applications from fusion to space science. [49, 48, 32, 8, 3, 25] Although the precise nature of transport phenomena may vary across applications, the underlying mathematical structure remains consistent. A significant challenge in solving transport equations is the associated computational cost, given that a general solution spans seven dimensions: three spatial coordinates, two angles, one energy (or speed), and one time. As the number of dimensions increases, the memory and computational resources required scale exponentially, limiting the feasibility of traditional numerical methods. The challenge has been aptly described by F. Graziani and G. Olson as "Conquering the Seven-Dimensional Mountain" [26].

To establish a robust computational framework, we focus on a fundamental yet representative model of transport phenomena: the linear, time-dependent, convection-diffusion-reaction Partial Differential Equation (PDE). We consider the PDE:

$$\frac{\partial f}{\partial t} - \varepsilon \Delta_{\mathbf{x}} f + \boldsymbol{\beta} \cdot \nabla_{\mathbf{x}} f + \rho f = b, \qquad \forall (\mathbf{x}, t) \in \Omega \times]0, T] \ , \tag{1}$$

The equation describes the evolution of the distribution function $f(\mathbf{x}, t)$ in the seven-dimensional phase space $\Omega \times [0, T]$, with $\mathbf{x} = (x_1, x_2, \ldots, x_d)^T \in \Omega \subset \mathbb{R}^d$, $d = 6$. Time is represented by $t \times [0, T]$ and

x_1, x_2, x_3 refer to the 3-D spatial variables. Depending on the specific form of equation (1) x_4, x_5, x_6 either describe the momentum vector or x_4, x_5 represent the 2-D angular direction of flight, and x_6 the energy or speed. The computational domain $\Omega \subset \mathbb{R}^d$ is the d-dimensional, open hypercube with characteristic edge length L and five-dimensional boundary Γ. To have a mathematically well-posed model, we assume that f satisfies Dirichlet boundary conditions on the domain boundary

$$f = g \quad \text{on } \Gamma \times [0, T], \tag{2}$$

and an initial condition at $t = 0$

$$f(\cdot, 0) = f_0 \quad \text{in } \Omega. \tag{3}$$

In Eq. (1), ε is the diffusion coefficient, $\boldsymbol{\beta}$ is the convection field, ρ is the reaction field, and b is the right-hand side forcing term. As a matter of notation, in the latter we drop the $\mathbf{x}$ subscript in the differential operators notation: $\nabla_{\mathbf{x}}$ becomes ∇ and $\Delta_{\mathbf{x}}$ becomes Δ.

The numerical solution of high-dimensional problems in the framework of Partial Differential Equations (PDEs) faces a fundamental challenge often referred to as the *curse of dimensionality* [4], where both memory requirements and computational costs scale exponentially with the number of dimensions. This is a serious limit for the effectiveness of numerical methods. While recent approaches have attempted to address this challenge through GPU acceleration [16] and machine learning methods [50, 42], these solutions introduce further complexities, as they require either architecture-specific programming or extensive training data.

To address these computational challenges, we take a different path based on a three-level approach. First, we operate in the context of the *low-rank approximation*[17]. We adopt the Tensor Train format [40], a linear algebra framework capable of efficiently handling high-dimensional data and mathematical operators, organized on tensor-product grids. Considerable effort has been devoted over the years to solving PDEs in Tensor Train format. Dolgov and coauthors tackled the three-dimensional Fokker-Planck equation [12]. Basic numerical schemes, such as uniform finite differences applied to the high-dimensional Poisson equation, are commonly used as testbed for the development of the Tensor Train linear system solvers [13, 14]. A hybrid approach for parametric PDEs in two dimensions can be found in [15]. In the context of semi-Lagrangian solvers, where special care has to be devoted to conservation of mass, energy, or momentum, Kormann [34] proposed a Tensor Train solver for Vlasov Equations.

Second, we numerically discretize the problem (1) using a variant of Spectral Collocation methods. The term "collocation" indicates that the continuous model, i.e. the PDE, is evaluated, "collocated", at specific grid points. These techniques are known for their long-recognized exceptional *accuracy* [6, 27], commonly exhibiting an exponential rate of convergence for smooth solutions. This rate of convergence is also addressed as spectral accuracy. However, their application to higher-dimensional problems, in standard algebra format, has been constrained by the dense structure of the discrete operators and the complexity of solving the resulting linear systems [6, 19].

Third, these methods face a fundamental trade-off between *accuracy* and *stability* [2, 18]. This becomes particularly problematic in regimes dominated by first-order derivatives ($\varepsilon/|\boldsymbol{\beta}L| \ll 1$), where solutions present spurious oscillations that make the result unreliable. Funaro's concept of superconsistency [20] cures such oscillations by performing collocation on modified nodes. The new position of the nodes is a function of the ratio $\varepsilon/|\boldsymbol{\beta}L|$ and the grid density [19, 11, 10]. We should note that superconsistency alone does not reduce the computational costs; the solution of high-dimensional problems remains prohibitive.

Our approach, **Tensor Train Superconsistent Spectral** ($\mathrm{T^2S^2}$), builds on the three techniques described above. It addresses the limitations of each individual block through a novel dimension-wise application of the superconsistent method. This approach fundamentally redefines the original superconsistent framework, making it compatible with the Tensor Train format and enabling an efficient storage of the mathematical operators. The method preserves the hallmark exponential accuracy of Spectral Collocation methods, while maintaining the stabilization properties with respect to the $\varepsilon/|\boldsymbol{\beta}L|$ ratio. At the same time $\mathrm{T^2S^2}$ achieves extremely low compression ratios, such as $\mathcal{O}(10^{-12})$, as a result, it can solve high-dimensional transport problems in minutes on standard hardware, rendering previously intractable problems computationally feasible.

The paper is organized as follows. The first section, "Overview of the $\mathrm{T^2S^2}$ Approach", presents the method, followed by the second section, "Results", which demonstrates the validation of the method through numerical experiments. The third section, "Discussion", summarizes the method's strengths, applications and future directions. The fourth section, "Methods", provides the detailed mathematical framework underlying the $\mathrm{T^2S^2}$ solver.

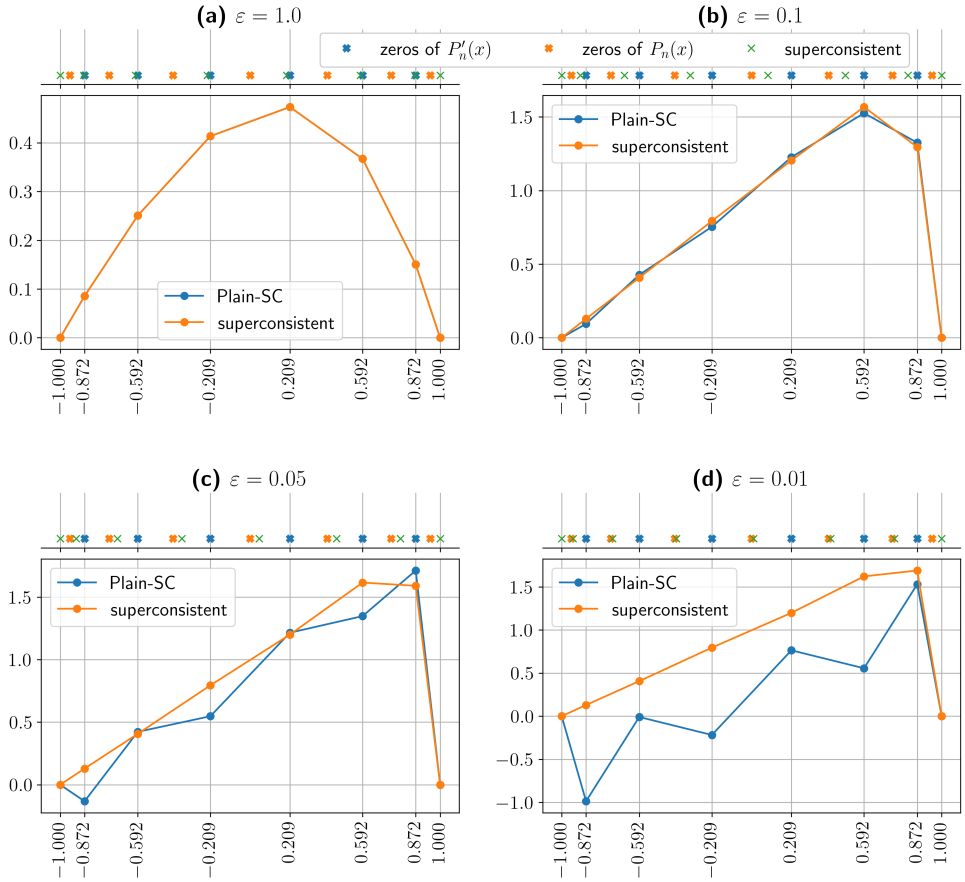

Figure 1: Superconsistent approximation of Eq.(4) for the polynomial degree $n = 7$, and $\beta = 1$. On the top horizontal axis, the blue crosses mark the zeros of P_n', optimal for diffusion; the orange crosses mark the zeros of P_n, optimal for convection; the green crosses mark the superconsistent collocation points for mixed regimes. Panels **(a)** and **(b)** show relatively accurate solutions when convection and diffusion are balanced, in particular in panel **(a)** the two solutions almost coincide. As convection dominates (panels **(c)** and **(d)**), the Plain-SC solution is unreliable, whereas the superconsistent one does not present problems.

Overview of the T^{2}S^2 Approach

This section outlines the key components of our methodology and demonstrates how they synergize to create our computational framework. We illustrate the underlying principles through one- and two-dimensional examples, while the detailed mathematical framework is provided in Section "Methods".

(i) ***Spectral collocation methods.*** Spectral collocation relies on two fundamental elements: *basis functions* and *representation points*. We employ Lagrange basis functions defined on $n+1$ representation points [19], which are the $n-1$ zeros of P_n', the derivative of the n-th degree Legendre polynomial P_n, complemented with the two extrema of the interval $[-1, 1]$. We will refer this approach as *plain spectral collocation* (Plain-SC) method. The solution to a one-dimensional transport problem is a linear combination of these basis functions. The coefficients are determined by solving the linear system obtained by *collocating the equation* at the same representation points, i.e., by evaluating the left-hand side and the right-hand side of Equation (1) at such locations. For nomenclature clarity, in one dimension, the number of degrees of freedom (#dofs) equals $n+1$. The multidimensional extension of the method is achieved through the tensor product of the one-dimensional discretizations along all the problem's directions.

(ii) ***Superconsistent formulation.*** To illustrate the concept of superconsistency we consider the time-independent one-dimensional model

$$\beta f'(x) - \varepsilon f''(x) = 1 \quad x \text{ in } \big[-1, 1\big], \quad f(-1) = f(1) = 0, \tag{4}$$

where $\beta > 0$ and $\varepsilon > 0$ are the scalar convective and diffusion coefficients, respectively. The Plain-SC method, employing the zeros of P_n', (blue dots on the top axis of Figure 1), develops spurious oscillations

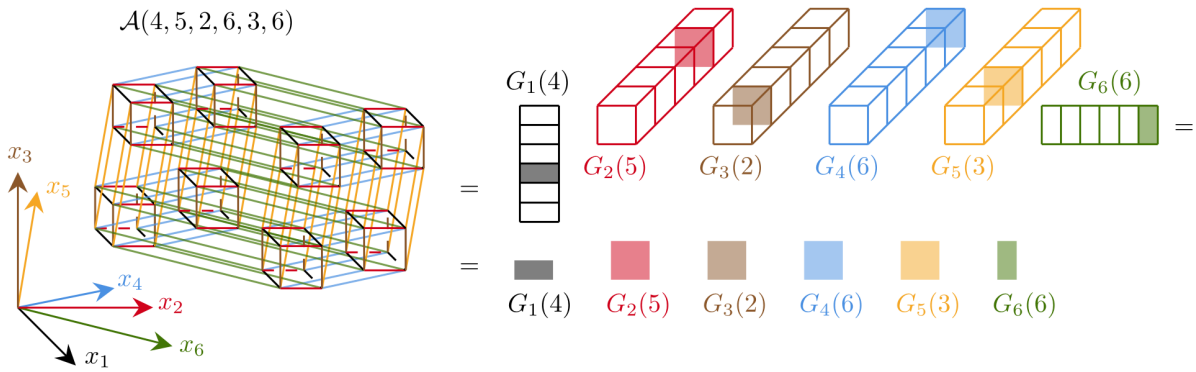

Figure 2: Focusing on the six spatial dimensions, a six-dimensional array $\mathcal{A}$ has size n^6, with $x_1, x_2, \ldots, x_6$ coordinate axis of the six-dimensional space. The TT format represents the whole array on the left as the product of six cores on the right. The ℓ-th core for $\ell = 1, 2, \ldots, 6$ has size $r_{\ell-1} \times n \times r_\ell$, with $r_0 = r_6 = 1$, so the first and last cores are matrices. The $(4, 5, 2, 6, 3, 8)$-th entry of the full tensor is represented in the TT-format as the product $\mathcal{A}(4, 5, 2, 6, 3, 8) = G_1(4)G_2(5)G_3(2)G_4(6)G_5(3)G_6(8)$, i.e., as the product of the 4-th, 5-th, 2-nd, 6-th, 3-rd, 8-th slices of the corresponding cores.

when the convective term becomes dominant relatively to the diffusive one, meaning that $\varepsilon/|\boldsymbol{\beta} L| \ll 1$. This effect is clearly visible in panels **(c)** and **(d)** of Figure 1.

Funaro [20] cured this phenomenon by introducing the superconsistent condition. The superconsistent condition takes into account the differential operator and is satisfied by introducing a different set of *collocation points* where the partial differential equation and the right-hand side are evaluated.

According to the superconsistent condition, the zeros of P_n' are optimal for the approximation of the diffusion operator $\varepsilon f''$, while the zeros of P_n are optimal for $\beta f'$. In hybrid regimes, the superconsistent points establish an optimal intermediate distribution between these two configurations. As illustrated in Figure 1, when convection and diffusion terms are balanced (Figure 1**(a)**), the superconsistent points are close to the zeros of P_n'. As the diffusion coefficient ε decreases maintaining n fixed (Figure 1**(b)** and **(c)**), the superconsistent points shift towards the zeros of P_n. In the convection-dominated regime (Figure 1**(d)**), the superconsistent points nearly coincide with the zeros of P_n.

In summary, the superconsistent approach is based on two grids: the *representation grid* and the actual *collocation grid*. The position of the collocation grid depends on the ratio $\varepsilon/|\boldsymbol{\beta} L|$ and n. Enforcing the superconsistent condition provides the numerical strategy to locate the collocation points in order to achieve stabilization with respect to $\varepsilon/|\boldsymbol{\beta} L|$. We use the representation points to build the Lagrange basis functions. These basis functions are used to evaluate the discrete operators at the collocation grid. The result of this *collocation* operation, together with boundary conditions, leads to the construction of the final linear system.

(iii) ***Tensor-train format.*** Traditional spectral methods struggle with the *curse of dimensionality* [4], where computational complexity increases by scaling exponentially with the number of dimensions. The Tensor-train (TT) format[40] efficiently represents a d-dimensional tensor as the product of d three-dimensional arrays, the *TT cores*, significantly reducing the memory requirement. Each tensor-train core, denoted by G_ℓ and indexed by $\ell = 1, 2 \ldots, d$, has dimensions $r_{\ell-1} \times n_\ell \times r_\ell$, where n_ℓ is the original dimension size also called the *mode size*, and r_ℓ are the *TT-ranks* (with $r_0 = r_d = 1$). As shown in Figure 2 for a six-dimensional tensor, an element of the multidimensional array $\mathcal{A} \in \mathbb{R}^{n_1 \times \ldots n_6}$ is reconstructed by multiplying the corresponding core slices $G_\ell \in \mathbb{R}^{r_{\ell-1} \times n_\ell \times r_\ell}$, $\ell = 1, 2, \ldots, 6$. The TT decomposition is not unique and is most effective when the TT-ranks are much smaller than the mode size, i.e., for $r_\ell \ll n_\ell$. In such a case, this method efficiently compresses large multidimensional arrays and, when applied to operators, mitigates the high bandwidth issue arising from tensor products.

We build the $\mathrm{T^2S^2}$ solver combining principles (i), (ii), and (iii) to extend superconsistency to high-dimensional equations. Our approach implements the superconsistent condition independently along each dimension, treating them as decoupled problems. This formulation works with two distinct time integration frameworks: the *unified space-time formulation*[46] that handles time as an additional dimension, and the *method-of-lines formulation*[44, 30] that uses conventional time-stepping schemes. For the latter, we implement the Crank-Nicholson and the backward Euler schemes. Highly accurate variants of these schemes, such as [43] are combinations of the mentioned methods. Superconsistency is applied only to the six spatial dimensions, demonstrating an oscillatory-free performance with respect to the ratio $\varepsilon/|\boldsymbol{\beta} L|$.

In Figure 3 we show a two dimensional grid obtained using $\mathrm{T^2S^2}$. The resulting Cartesian structure

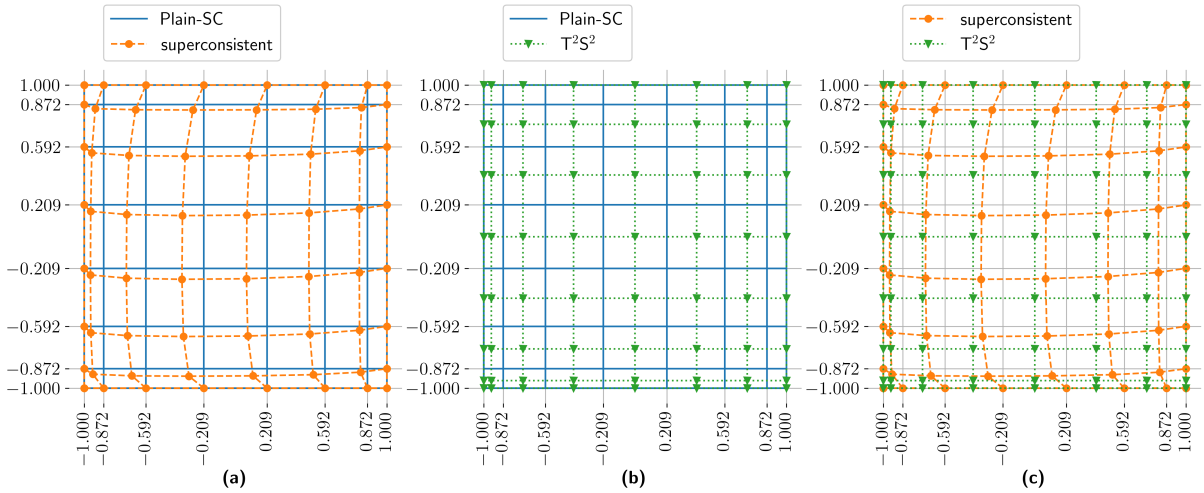

Figure 3: Left panel: Plain-SC nodes and Funaro's superconsistent nodes[19]. Such a grid has been evaluated for problem (4) with parameters $\varepsilon = 1/50$, $\beta = (1, 0.5)^T$ and $n = 7$. Middle panel: Plain-SC nodes and T^2S^2 collocation nodes, which have been independently computed in each direction. Right panel: Comparison between the 2D Funaro's superconsistent nodes[19] and T^2S^2 collocation nodes.

naturally fits with the tensor-train format and extends straightforwardly to higher dimensions. This approach differs from Funaro's original formulation[19] , which applies superconsistency to the full multidimensional problem and produces non-Cartesian grid deformations, see Fig. 3. Our method is stable across physically relevant parameter ranges and preserves the exponential accuracy that is characteristic of the spectral collocation methods.

Results

In this section, we analyze the T^2S^2 performance from various perspectives. First, we assess its accuracy and convergence by investigating its behavior when approximating a low-rank, high-frequency analytical solution. The high-frequency test examines T^2S^2's performance on a grid density with $300^7 \approx 2.2\,10^{17}$ nodes that can only be explored by low-rank solvers since a full format traditional solver, even at minimal complexity would require millions of years on modern supercomputers. Next, we present a six-dimensional test case that triggers the $\varepsilon/|\boldsymbol{\beta} L| \ll 1$ instabilities when we approximate a high-gradient solution that challenges the low-rank approximation on moderate to high-density grids. It tests the robustness of T^2S^2 in handling such instabilities. Finally, we complete our investigation with two low-dimensional test cases that challenge the non-oscillatory performance of the T^2S^2 solver: the "traveling bump" benchmark [19, 22] and the Hughes double-layer benchmark [29, 5].

Global Accuracy and Computational Cost

Testing numerical algorithms with manufactured analytical solutions is a cornerstone practice in numerical analysis. It provides a reliable way to create benchmark solutions for validating numerical solver[37]. In this case, we construct an "exact" solution by choosing a suitable expression, and we determine the corresponding right-hand side analytically. To this end, we apply our T^2S^2 solver to problem (1)-(3) on $\Omega \times [0, T]$ with $\Omega = [-1, 1]^6$ and $T = 1$. For convenience, we rescale the time interval to match the interval $[-1, 1]$. We set $\varepsilon = 10^{-4}$,

$$\boldsymbol{\beta}(x_1, x_2, \ldots, x_6) = (\sin(\pi x_1), \sin(\pi x_2), \ldots, \sin(\pi x_6))^T,$$

$$\rho(x_1, x_2, \ldots, x_6) = \prod_{1 \le i \le 6} \left[\frac{1}{2} - \left(x_i + \frac{11}{10}\right)\left(x_i - \frac{1}{2}\right)\left(x_i + \frac{1}{2}\right)\left(x_i - \frac{11}{10}\right) \right].$$

The right-hand side b and the Dirichlet boundary conditions are determined from the proposed analytical solution:

$$f(\mathbf{x}, t) = e^t \cdot \prod_{1 \le i \le 6} \left(\sin(\pi x_i) + 0.3 \sin(80 \pi x_i)\right).$$

Here, we test the space-time formulation. In this setting, the initial condition is naturally incorporated as a boundary condition at $t = -1$, while at $t = 1$, the numerical solution is a result of the numerical scheme. The analytical solution $f(\mathbf{x}, t)$ incorporates two spatial components: a low-frequency one, i.e. $\sin(\pi\cdot)$, that spans the computational domain, and a high-frequency one, i.e. $\sin(80\pi\cdot)$, that introduces features at approximately 1/100 of the domain size. Such multi-scale phenomena are commonly encountered in practical applications [23, 47].

The results are presented in Figure 4. Each "dot" represents an approximation of the solution of problem (1) for a given polynomial degree (associated with the number of degrees of freedom). The convergence tests are based on the following L^2-type error norm:

$$\text{error} = \frac{\|f - f_n\|_{\mathcal{F}}}{\|f\|_{\mathcal{F}}},$$

where $\|,\cdot,\|_{\mathcal{F}}$ denotes the Frobenius norm and f_n represents the polynomial approximation of degree n of the solution f.

Panel (**b**) shows that we need a grid of approximately 256^7 size to capture the two dominant frequencies of the solution. From that point onwards, we can appreciate the exponential decay of the error characteristic of the spectral methods. The solver achieves an $\mathcal{O}(10^{-11})$ approximation error for a grid size having a total number of 300^7 nodes (including time). Panel (**a**) shows that $\mathrm{T^2S^2}$ achieves the desired accuracy in under three minutes on an Intel i9 laptop computer with 64 GBytes RAM. We put this number into perspective theorizing a full format Super Spectral Collocation solver with minimal quadratic complexity $((\#\mathsf{dofs})^7)^2$, labeled *full format solver*, [20, 19]. We estimate that a modern supercomputer, characterized by a peak performance of 2.7^{18} floating point operations per second[38], would require approximately fifty million years to run the full format solver on the 256^7 grid. The computational cost for the first grid that exhibits spectral accuracy, the one with 300^7 total degrees of freedom, would approximately be 300 million years. These two timescales respectively compare with the geological age of the Himalayas and the Dolomites. These results are a consequence of the fact that $\mathrm{T^2S^2}$ can capture a low-rank solution of a maximum rank of 9, resulting in a compression ratio of $(7 \cdot 9^2 \cdot 300)/300^7 = \mathcal{O}(10^{-12})$. The corresponding memory requirement for the full format solver exceeds one exabyte, indicated by the arrow in Figure 4-(**a**). One exabyte compares at best, or exceeds, the storage capacity of todays largest supercomputers [38].

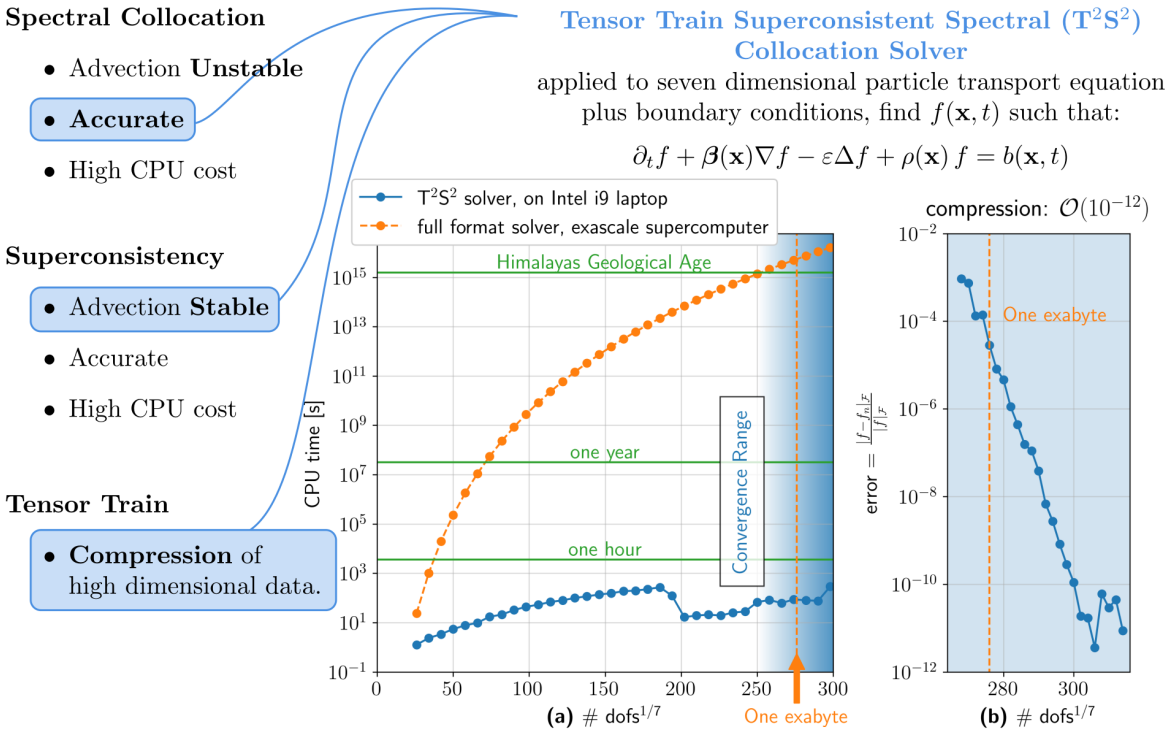

Figure 4: This figure showcases the key components of T^2S^2 and its performance in solving the manufactured transport problem. Panel (**a**) illustrates T^2S^2's compression capabilities, which enable the real-time solution of a seven-dimensional space-plus-time problem. To convey to the reader the scale of the performance, we provide a comparison with the estimated computational time for a full format solver with minimal numerical complexity [19, 6], whose cost scales as $\mathcal{O}((\#\mathsf{ndofs})^7)^2$. Assuming such a full format solver runs on a 2.7 exaFLOPS nominal supercomputer, the projected execution time would be on the order of fifty million years, comparable to the geological age of the Himalayas. An arrow is used to indicate the "One exabyte" memory for the full format solver. Panel (**b**) shows the convergence behavior. The error decreases exponentially, eventually reaching machine precision.

Figure 5 shows the convergence analysis of T^2S^2 on a six-dimensional, constant coefficient test case. We set $\varepsilon = 10^{-6}$, $\boldsymbol{\beta}$ as a six-dimensional unit vector and $\rho = 0$. The analytical solution is prescribed as

$$f(\mathbf{x}, t) = e^{-t} \cdot \prod_{1 \le i \le 6} (\sin(\pi x_i)) \,,$$

from this, we derive the corresponding right-hand side and boundary condition for the discrete model. Figure 5 presents the error curve as a function of the number of degrees of freedom along one dimension. The results demonstrate that the method preserves spectral accuracy.

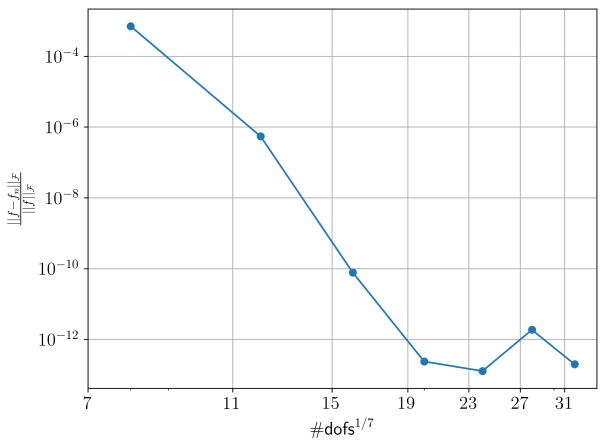

Figure 5: This convergence curve shows the exponential decay of the approximation error of the numerical solution versus the number of degrees of freedom in each direction from the application of $\mathrm{T}^2\mathrm{S}^2$ to a seven-dimensional convection-diffusion problem with velocity field $\boldsymbol{\beta} = (1, 1, \ldots, 1)^T$ and diffusion coefficient $\varepsilon = 10^{-6}$.

Superconsistent Stabilization of Convection-Dominated Problems

Stabilization techniques for convection-diffusion problems have been extensively studied in the literature[29, 5], mainly focusing on low dimensional stationary convection-diffusion equation with Dirichlet boundary conditions. We consider a six dimensional equivalent:

$$\begin{aligned} -\varepsilon\Delta f + \boldsymbol{\beta}\cdot\nabla f &= b \quad \text{in } \Omega, \\ f &= 0 \quad \text{on } \partial\Omega. \end{aligned} \tag{5}$$

This equation is a specialized case of our target problem (1), which we analyze on the six-dimensional hypercube domain $\Omega = [-1, 1]^6$. Conventional spectral approximations perform effectively in diffusion-dominated regimes where $\varepsilon\Delta f$ predominates over $\boldsymbol{\beta}\cdot\nabla$. However, they exhibit spurious oscillations in convection-dominated scenarios which are common in many practical applications[23, 45].

For our numerical experiments, we take $b = 1$ and define $\boldsymbol{\beta}$ as a vector of ones. The right-hand side is set as the identity function, and homogeneous boundary conditions are applied. In Figure 6, we vary the degree of the space discretizations and ε. We compare $\mathrm{T}^2\mathrm{S}^2$ with the Plain-SC stored in tensor train format, we label this method Plain-SC-TT. The results are displayed on colormaps (**c**) and (**d**), where red pixels indicate an oscillatory solution; green pixels represent a non-oscillatory solution. We count the number of sign changes in the first derivative of the numerical solution. We compare this number with the expected sing changes in the regular solution. If the first count exceeds the second, the solution is marked as oscillatory. Oscillations are evaluated on the mid-axis along the first direction, at the center most degree of freedom.

Panels (**a**)-(**b**) of Figure 6 show a two-dimensional slice of the six-dimensional solution computed with $\varepsilon = 10^{-5}$ and 40 degrees of freedom. Panel (**b**) presents the non-oscillatory solution, which exhibits a continuous profile with a well-resolved boundary layer at the domain perimeter. In contrast, panel (**a**) shows the oscillatory solution, where spurious oscillations dominate the numerical approximation, rendering the spatial discretization ineffective. Colormap in Figure 6-(**c**) shows that the Plain-SC-TT approach is unstable for a wide range of parameters. The stable/unstable interface follows a precise law; diffusive terms scale like $\mathcal{O}(\#\mathsf{dofs}^4)$, while transport terms scale like $\mathcal{O}(\#\mathsf{dofs}^2)$, see Section "Methods".

It is, in principle, true that even for a very small value of $\varepsilon/|\boldsymbol{\beta}L|$, we can find a sufficiently refined mesh where the diffusion term becomes numerically dominant, and the Plain-SC-TT approximation is stable. This approach is unfortunately illusive, since it is always possible to choose smaller values of $\varepsilon/|\boldsymbol{\beta}L|$ that result in spurious oscillations in the solution. Moreover, the computational capability of Tensor Train linear solvers is remarkable but not infinite. AMEn[13], an advanced TT linear system solver requires solving local problems at each TT core iteration, with each local direct solution having complexity $\mathcal{O}((r_{\ell-1}, n_\ell, r_\ell)^3)$, where $r_{\ell-1}, r_\ell$ denote the TT ranks and n_ℓ the mode size of the corresponding core. This results in a challenging computational limit on the maximum possible resolution determined by the hardware's RAM. This is why $\mathrm{T}^2\mathrm{S}^2$ comes into play. The super-consistent discretization is always unconditionally stable regardless of the choice of the parameters; see Figure 6-(**d**).

The boundary layer in Figure 6-(**b**), characterized by a high gradient connecting the domain solution

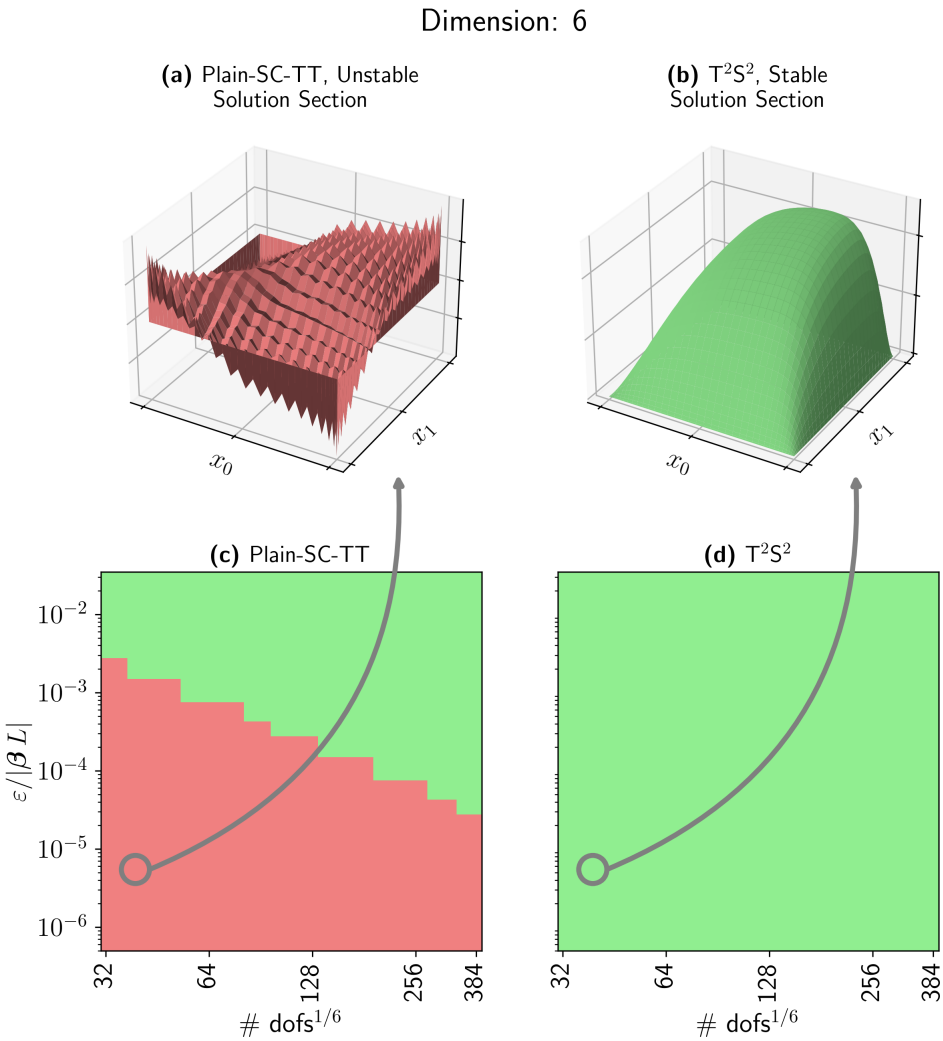

Figure 6: With $\boldsymbol{\beta}$ fixed as a six-dimensional unit vector, we conduct a detailed analysis of the solution's oscillatory behavior. Panel (**a**) shows a two-dimensional cross-section of the solution to the six-dimensional problem (5) with $\varepsilon = 10^{-5}$ and polynomial degree 39, using collocation points at the zeros of P_n'. The solution presents macroscopic spurious oscillations. The corresponding solution using superconsistent collocation points exhibits the expected regularity and characteristic boundary layers. Panels (**c**) and (**d**) present colormaps where each pixel represents a discrete solution of problem (5) for specific combinations of polynomial degree and $\varepsilon/|\boldsymbol{\beta} L|$. Panel (**c**) highlights regions of oscillatory solutions in red, demonstrating the limitations of Plain-SC-TT. In contrast, panel (**d**) illustrates how our method maintains non-oscillatory behavior across all values of $\varepsilon/|\boldsymbol{\beta} L|$ and polynomial degrees.

to the zero boundary condition challenges the rank compression of the Tensor Train format, as higher gradients typically result in a more dense solution structure in terms of dominant patterns [35].

In Figure 7, we relate the linear solver "iterations" to the Tensor Train ranks, compression factors, and residuals for T^2S^2 and Plain-SC-TT. The Tensor train solver is AMEn[13], ant the "iterations" are addressed as swaps in the tensor train nomenclature.s Panel (**b**) illustrates that the tensor-train solver adjusts the solution rank with each swap, reaching a stationary point at swap 11 with a rank of 11. At this point, both our method and the Plain-SC-TT approach reach their resolution limit, and beyond it, they are unable to extract further information. Maximum rank 11 corresponds to a compression factor around $\mathcal{O}(10^{-6})$, cf. the details in panels (**b**) and (**c**). Although T^2S^2 and Plain-SC-TT achieve a similar compression ratios, their convergence properties diverge substantially. The residual analysis in panel (**c**) reveals that T^2S^2 maintains consistent convergence with regular residual decay while Plain-SC-TT exhibits non-convergent behavior characterized by irregular residual patterns. The final residual value of $\mathcal{O}(10^{-2})$ reflects the problem's poor conditioning [20, 6]. Moreover, the computational cost of T^2S^2 for solving a problem with $\#\mathsf{dofs} = \mathcal{O}(10^9)$ on an Intel i9 laptop computer is in the range of seconds.

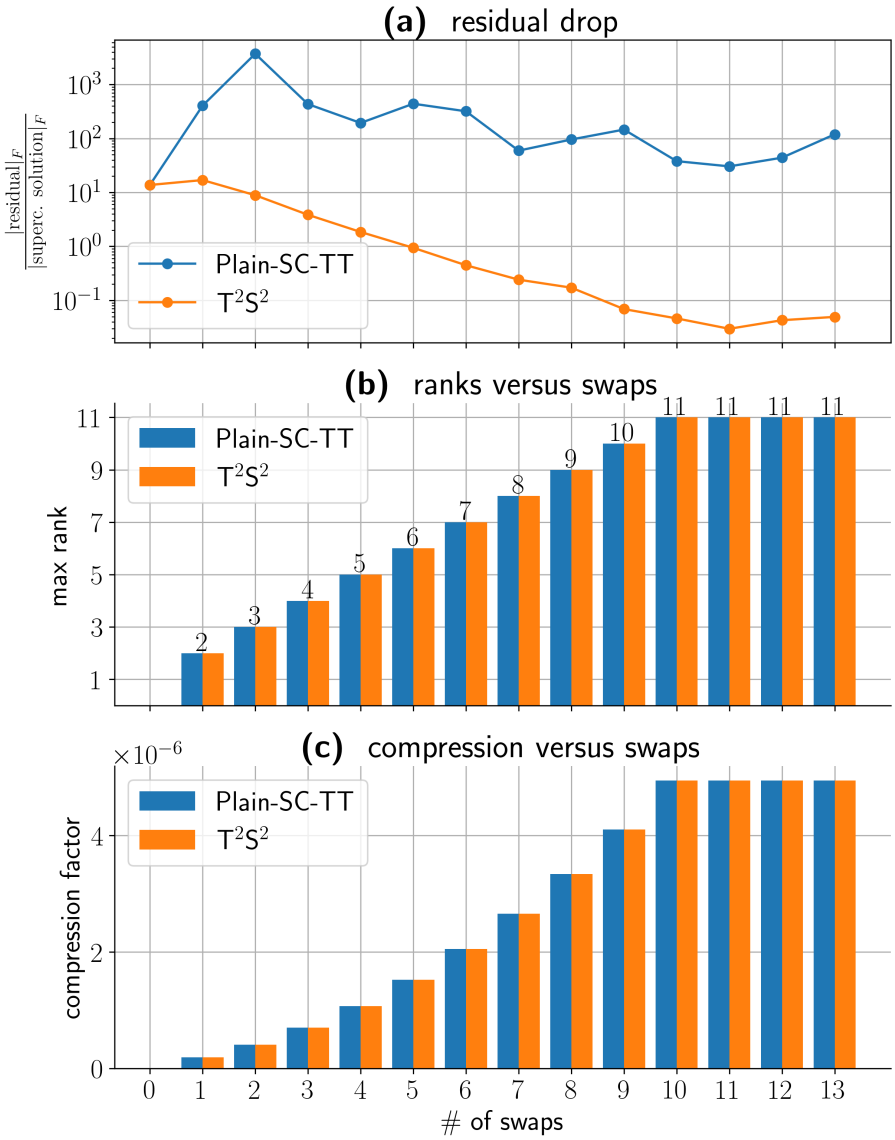

Figure 7: We present the residual decay, the ranks, and the compression factor against the number of AMEn swaps [13] for our T^2S^2 solver and the Plain-SC-TT collocation methods in the case of 6 dimensional problem 5, degree 39, $\varepsilon = 10^{-5}$ and $\boldsymbol{\beta}$ six-dimensional vector of ones. This problem is of special interest because it presents a boundary layer. The boundary layer is a high-gradient region of the solution that connects a boundary condition with the internal values. The approximation of such high gradients is generally challenging in the tensor train format. Panel (**a**) reports how the residual drops against the number of swaps. The residual does not converge in the Plain-SC-TT case, while in T^2S^2 case, the residual drops with a regular gradient. The final value of the residual $\mathcal{O}(10^{-2})$ is a consequence of the overall bad conditioning of the problem. Panel (**b**) shows that the solver increases the rank of the solution at each swap until it finds a stationary point at swap 11 for a corresponding rank equal to 11. After the 11th swap, the solver does not find any further information. The compression factor is in the range of $\mathcal{O}(10^{-6})$, (**c**). The computational cost on an i9 Intel laptop with 64 Gigabytes of RAM is in the range of seconds.

Low-Dimensional Numerical Challenges

This section presents two low-dimensional test cases to assess the characteristic capabilities of $\mathrm{T^2S^2}$. The first test is the traveling bump benchmark [22, 19]. The bump benchmark is a two-dimensional time-dependent problem where the initial condition is known, but there is no a priori knowledge of the evolution of the solution. The test is based on a rotational velocity flow, that challenges the Cartesian structure of the $\mathrm{T^2S^2}$ grid. Although we choose collocation points to be the zeros of P_n, considering positive convection coefficients in both directions, $\mathrm{T^2S^2}$ nonetheless proves to be robust. We solve problem (1)-(3) with $\boldsymbol{\beta} = (-x_2, x_1)^T$, $\varepsilon = 10^{-6}$ and $\rho = 0$. The space-time domain is given by $\Omega \times T = ([-1,1] \times [-1,1]) \times [0,\pi]$. The initial condition is:

$$f(x_1, x_2, 0) = \begin{cases} 16\left(1 - 4\left(x_2 - \frac{1}{2}\right)^2\right)^2 \left(1 - 4\,x_1^2\right)^2 & x_2 > 0,\ \frac{1}{2} \le x_1 < \frac{1}{2}, \\ 0 & \text{elsewhere.} \end{cases}$$

The polynomial degree of the basis functions is 16. Figure 8 presents the results of this calculation, in the case of the spacetime formulation. Panel (**a**) illustrates the evolution of the bump's position within the domain, which describes a circular trajectory through contour lines at various time snapshots, together with the prescribed velocity field. Theoretically, the configuration at time π should be mirror symmetric versus the initial condition. Panel (**b**) provides quantitative accuracy analysis through the normalized maximum norm $\|f_n(\cdot, t_i)\|_\infty/16$, computed on a 128×128 uniform grid. The results demonstrate that $\mathrm{T^2S^2}$ preserves the solution structure with minimal oscillation behavior. In this panel we superimpose the result for the spacetime formulation and the time marching schemes: backward Euler and Crank-Nicolson. The implicit backward Euler scheme reads:

$$f^{k+1} - \Delta t\Big(\varepsilon \Delta f^{k+1} - \boldsymbol{\beta} \cdot \nabla f^{k+1}\Big) = f^k, \tag{6}$$

and the semi-implicit Crank-Nicolson scheme is:

$$f^{k+1} - \frac{\Delta t}{2}\Big(\varepsilon \Delta f^{k+1} - \boldsymbol{\beta} \cdot \nabla f^{k+1}\Big) = f^k + \frac{\Delta t}{2}(\varepsilon \Delta f^k - \boldsymbol{\beta} \cdot \nabla f^k). \tag{7}$$

We choose a time step $\Delta t = \pi/160$ in both cases. Since the implicit backward Euler scheme is only first-order accurate, the solution approximation shows significative numerical diffusion as the peak's value is reduced by roughly 10%. The Crank-Nicolson scheme is particularly well-suited for this problem due to its reduced numerical dissipation compared to fully implicit schemes. This property is critical as it better preserves the system's physical quantities, which is a key characteristic in many applicative problems.

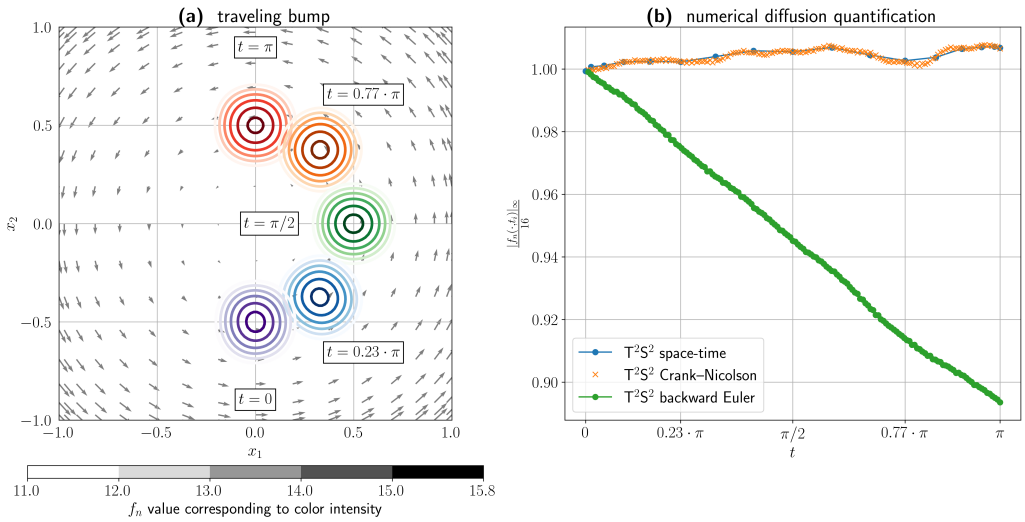

Figure 8: Results for the traveling "bump" test case. Panel (**a**) shows contour lines for the "bump" at different time steps. Different colors distinguish the different instants; the shades distinguish the different function values. The different levels are reported in the gray color bar. Panel (**b**) shows the time evolution of the solution peak values for three $\mathrm{T^2S^2}$ method's implementations using the implicit backward Euler scheme, the semi-implicit Crank-Nicolson scheme, and the space-time formulation. A video of the traveling bump is provided as Supplementary Materials.

The second test case, originally proposed by Tom Hughes and coauthors [29, 5], evaluates the method's ability to resolve both boundary and internal layers. We solve problem (5) in two dimensions with $b = 0$

and decreasing values of ε. The discontinuous boundary at $x_2 = 0$, which is transported in the interior by the convection field $\boldsymbol{\beta} = (1, 3)^T$, generates the internal layer on the bottom side of the computational domain. The boundary layer is determined by setting a homogeneous boundary condition on the top side of the computational domain. The test case specifics are sketched in Figure 9. The boundary layer connects the solution with the boundary conditions and the internal layer connects two flat regions of the solution, i.e., $f = 1$ (on the left), and $f = 0$ (on the right). The reader will notice that the smaller is ε, the higher is the gradient of the internal layer; see Figures 10-(**a**), 10-(**b**), 10-(**c**). T^2S^2 method confirms its oscillatory-free behavior. In contrast, Plain-SC method exhibits spurious numerical oscillations, Figures 10-(**d**), 10-(**e**), 10-(**f**), which start being visible for a relatively big value of $\varepsilon = 10^{-3}$, and fails to resolve the problem accurately.

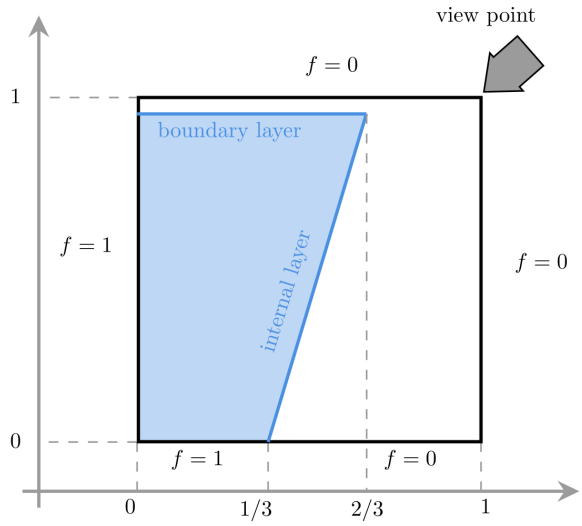

Figure 9: This picture gives a schematic overview of the convection-diffusion test case as proposed by Hughes and coauthors[29, 5], highlighting the boundary and internal layers of the solution.

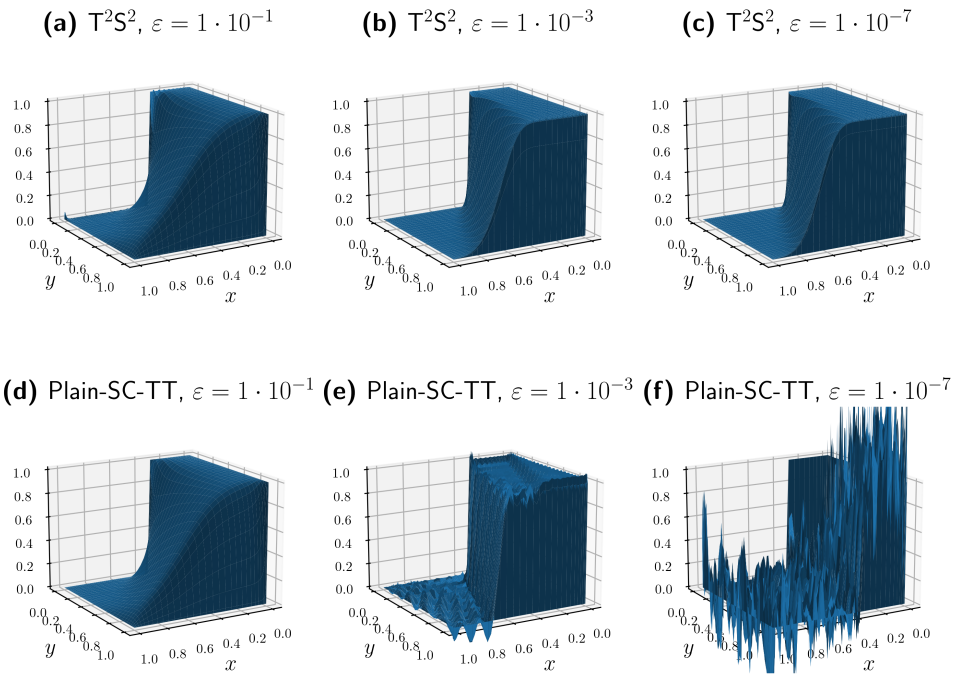

Figure 10: This picture represents the solutions of the test proposed by Hughes and coauthors [29, 5] for various values of the parameter ε and for the Plain-SC-TT collocation method versus T^2S^2. The solution degree is 63. While Plain-SC-TT shows spurious oscillations at $\varepsilon = 10^{-3}$, T^2S^2 is stable regardless of the value of ε.

Discussion

T^2S^2 effectively integrates the strengths of its core components: Spectral Collocation for accuracy, Superconsistency for stability and Tensor Train format as a low-rank linear algebra framework.

In Section "Results" , we demostrated that T^2S^2 reduces the approximation error to the range of the machine precision, with the error decreasing sharply when plotted on a logarithmic scale. Despite using a low-rank solution, the grid density is such that traditional solvers—even at theoretically optimal efficiency— would require millions of years on the current world's most powerful architectures.T^2S^2 preserves spectral accuracy in high-dimensional, high dense grid scenarios.

In the section about stability, we experimentally tested the solver's stability using a six-dimensional stationary test case characterized by a boundary layer solution, i.e., a solution characterized by a high gradient region connecting the domain interior to the homogeneous boundary conditions. This test not only confirms the unconditional stability of the method versus the parameters choice, but also shows that T^2S^2 can approximate high dimensional/high gradient solutions with a rank in the range of 10.

T^2S^2 achieves this without requiring any intermediate approximation layers, either at the continuous or discrete level: the discrete version of problem (1) fits naturally into the Tensor Train structure. Moreover, T^2S^2 differs fundamentally from low-rank data-driven approaches, such as machine learning and reduced-order modeling[36, 28], as it does not require any high-fidelity offline computations or training phases. As discussed in "Results" , we remarked that a high-fidelity computation in seven dimensions results in prohibitive computational costs, even for a relatively coarse grid.

Following the characterization of low-rank methods proposed in the comprehensive review by Einkemmer et al.[17], a time discretization of T^2S^2, such as the backward Euler and Crank-Nicholson schemes, falls into the category of the *Step And Truncate* (SAT) methods. SAT methods offer the flexibility to incorporate T^2S^2 into existing time marching schemes, while spacetime T^2S^2 performs the compression also along the time dimension.

Problem (1) serves as the basis for a wide range of solvers in fields such as radiation transport physics, kinetic theory, and computational fluid dynamics. As such, T^2S^2 is a tool for a wide range of applications in modeling high-dimensional transport phenomena. Technological advances are driving the development of next-generation nuclear technologies, including small modular reactors, advanced modular reactors, microreactors, and nuclear fusion systems. These innovations demand large-scale neutron transport and fluid dynamics calculations for reactor design and throughout the nuclear fuel cycle, including nuclear safeguards, nuclear non-proliferation, and security needs [41, 1, 31, 21, 7]. We expect T^2S^2 to be a key numerical solver in addressing these complex computational challenges.

Beyond nuclear applications, T^2S^2 has the potential to impact a wide range of fields requiring efficient, high-dimensional transport computations. Its ability to solve such problems on standard computing hardware makes it particularly valuable for practical applications with limited computational resources. Future directions include extending the T^2S^2 architecture to run efficiently on supercomputers, expanding its applicability to large-scale scientific and engineering problems.

Methods

In this section, we describe the Tensor Train format a fundamental building block for T^2S^2, alongside Spectral Collocation Methods [19], and Superconsistency [20].

Tensor Train representation

We first review some basic notation and definitions about tensors [33] and, in particular, the tensor-train format [39, 40]. Then, we review some important basic facts about the tensor-train decomposition.

Notation and generalities. A d-dimensional tensor $\mathcal{A} = \{\mathcal{A}(i_1, i_2, \ldots, i_d)\}$, $i_\ell = 1, 2, \ldots, n_\ell$, $\ell = 1, 2, \ldots, d$ is a multi-dimensional array whose entries are indexed by d indices. We denote d-dimensional tensors using calligraphic, upper case fonts, such as $\mathcal{A}, \mathcal{B}, \mathcal{C}$. For scalars, vectors, and matrices, which are formally d-way tensors with, respectively, a number of dimensions $d = 0, 1, 2$, we adopt a different notation for clarity. Precisely, we denote scalar quantities using normal, lower-case fonts as in a, b, c; vector fields using bold, lower-case fonts as in $\mathbf{a}, \mathbf{b}, \mathbf{c}$; matrices using normal, upper case fonts as in A, B, C. Furthermore, we denote the entries of a vector $\mathbf{a}$ as $a(i)$ and the entries of a matrix A as $A(i, j)$. We may occasionally denote the entries of three-dimensional tensor as $\mathcal{A}(i, j, k)$ instead of $\mathcal{A}(i_1, i_2, i_3)$, but we prefer using the notation $\mathcal{A}(i_1, i_2, \ldots, i_d)$ when $d > 3$. For completeness, we anticipate that when we consider a three-dimensional tensor that is also a core of a tensor train decomposition (see below for

the definition), the first and last indices are a Greek letter, e.g., α, β etc, and the intermediate index is always a Roman letter, e.g., i, j etc.

Following a MATLAB-style notation, we denote free indices using the symbol ":". This notation makes it possible to represent the two important structural concepts of *fiber* and *slice* of a tensor. A fiber is a vector obtained by fixing all but one index, and a slice is a matrix obtained by fixing all but two indices. For example, a 3D tensor $\mathcal{A}(i,j,k)$ has three different types of fibers, i.e., $\mathcal{A}(:,j,k)$, $\mathcal{A}(i,:,k)$, $\mathcal{A}(i,j,:)$, and three different types of slices $\mathcal{A}(i,:,:)$, $\mathcal{A}(:,j,:)$, $\mathcal{A}(:,:,k)$. Finally, always according with the MATLAB-style notation, a repetition of the free index symbol ":" denotes an index contraction. For example, let A, B, C be three matrices with compatible sizes such that $C = AB$. Then, the notation "$C(i,j) = A(i,:)B(:,j)$" is equivalent to $C(i,j) = \sum_\alpha A(i,\alpha)B(\alpha,j)$, where the summation over the index α is taken, as usual, over all the elements of the i-th rows of A and j-th columns of B.

Tensor-train format. The tensor-train format provides an efficient representation of high-dimensional tensors by decomposing them into a product of much smaller, three-dimensional tensors called the "TT cores". Specifically, a d-dimensional tensor $\mathcal{A} \in \mathbb{R}^{n_1 \times \cdots \times n_d}$ is said to be in tensor-train format if there exist d cores $\mathcal{A}_\ell \in \mathbb{R}^{r_{\ell-1} \times n_\ell \times r_\ell}$, for $\ell = 1, \ldots, d$, with $r_0 = r_d = 1$, such that each entry of $\mathcal{A}$ can be computed as:

$$\mathcal{A}(i_1, \ldots, i_d) = \sum_{\alpha_1=1}^{r_1} \cdots \sum_{\alpha_{d-1}=1}^{r_{d-1}} \mathcal{A}_1(1, i_1, \alpha_1)\mathcal{A}_2(\alpha_1, i_2, \alpha_2) \cdots \mathcal{A}_d(\alpha_{d-1}, i_d, 1). \tag{8}$$

In some sense, Equation (8) is a multi-dimensional generalization of the (reduced) Singular Value Decomposition (SVD) of matrices. Note, however, that we do not require any specific orthogonality property in the above definition (more details on the SVD connection will be given in the next example and later in this section).

To fix ideas, consider the following two dimensional case. A matrix $A \in \mathbb{R}^{n_1 \times n_2}$ is decomposed in the product of two matrices $A_1 \in \mathbb{R}^{n_1 \times r_1}$ and $A_2 \in \mathbb{R}^{r_1 \times n_2}$, so that $A(i_1, i_2) = \sum_{\alpha=1}^{r_1} A_1(i_1, \alpha)A_2(\alpha, i_2)$. We can easily construct such a decomposition through the SVD of A, which we write as usual as $A = U\Sigma V^T$, where $U \in \mathbb{R}^{n_1 \times r_1}$ and $V \in \mathbb{R}^{n_2 \times r_1}$ are two orthogonal-by-column matrices, and $\Sigma \in \mathbb{R}^{r_1 \times r_1}$ is the diagonal matrix with r_1 strictly positive singular values, so that r_1 is the rank of matrix A. Then, take, for instance, $A_1 = U$, $A_2 = \Sigma V^T$, or $A_1 = U\Sigma$, $A_2 = V^T$. We can also use the tensor notation introduced above and specialized to the case $d = 2$, so that we can write $\mathcal{A}(i_1, i_2) = \sum_{\alpha=1}^{r_1} \mathcal{A}_1(1, i_1, \alpha)\mathcal{A}_2(\alpha, i_2, 1)$, where $\mathcal{A}_1 \in \mathbb{R}^{r_0 \times n_1 \times r_1}$, $\mathcal{A}_2 \in \mathbb{R}^{r_1 \times n_2 \times r_2}$, with $r_0 = r_2 = 1$. The decomposition process can be easily extended to $d = 3$ by redefining $\mathcal{A}_2$ as the intermediate core $\mathcal{A}_2 \in \mathbb{R}^{r_1 \times n_2 \times r_2}$ and introducing a final core $\mathcal{A}_3 \in \mathbb{R}^{r_2 \times n_3 \times r_3}$ with $r_3 = 1$, so that $\mathcal{A}(i_1, i_2, i_3) = \sum_{\alpha_1=1}^{r_1} \sum_{\alpha_2=1}^{r_2} \mathcal{A}_1(1, i_1, \alpha_1)\mathcal{A}_2(\alpha_1, i_2, \alpha_2)\mathcal{A}_2(\alpha_2, i_3, 1)$. This process can be continued by adding one new dimension at each step as it is illustrated in Fig. 11 for the construction of the TT representation of a tensor up to $d = 6$.

Remark. The computational effectiveness of the TT representation of multi-dimensional arrays is related to controlling the core ranks. To exemplify this fact, consider a six-dimensional array with mode sizes $n = n_1 = \ldots = n_6 = 10^3$ and assume that the ranks are all equal to $r = r_1 = \ldots = r_{d-1} = 10$. In such a case, the total storage required to represent such a tensor in TT format is proportional to $\mathcal{O}(nr^2d) = 6\,10^5$ against a full grid storage requirement of $\mathcal{O}(n^d) = 10^{18}$.

The TT representation can equivalently be reformulated in a more compact form by representing each core as a set of slice matrices parametrized with the spatial index i_ℓ, e.g., $A_\ell(i_\ell) = \mathcal{A}_\ell(:, i_\ell, :) \in \mathbb{R}^{r_{\ell-1} \times r_\ell}$, yielding:

$$\mathcal{A}(i_1, \ldots, i_d) = A_1(i_1)A_2(i_2) \cdots A_d(i_d). \tag{9}$$

The internal sizes of the decomposition, i.e., the set of $(d-1)$ integers $\{r_\ell\}_{\ell=1}^{d-1}$, are the the *TT-ranks*, or, simply, the *ranks*, of the TT decomposition. A convenient upper bound on them is their maximum value, which we denote as $r = \max_\ell\{r_\ell\}$. We also introduce an upper bound on the dimensions, denoted as $n = \max_\ell n_\ell$. The TT-ranks determine the storage complexity of the representation, which scales linearly with the dimension d as $\mathcal{O}(dnr^2)$, in contrast to the exponential growth $\prod_{\ell=1}^d n_\ell = \mathcal{O}(n^d)$ required for the full tensor representation. The linear dependence on d of the TT-representation of a tensor is very convenient, reflecting the compression efficiency of such a representation, whenever $r \ll n$. In such a case, we say that (8) and (9) are a *low-rank representation* of tensor $\mathcal{A}$.

If we introduce the multi-index $i = (i_1, i_2, \ldots, i_d)$, we can think that Equation (8) defines the TT format representation for a sort of "*multi-dimensional vector*", i.e., $\mathcal{A}(i)$. It is also possible to adopt

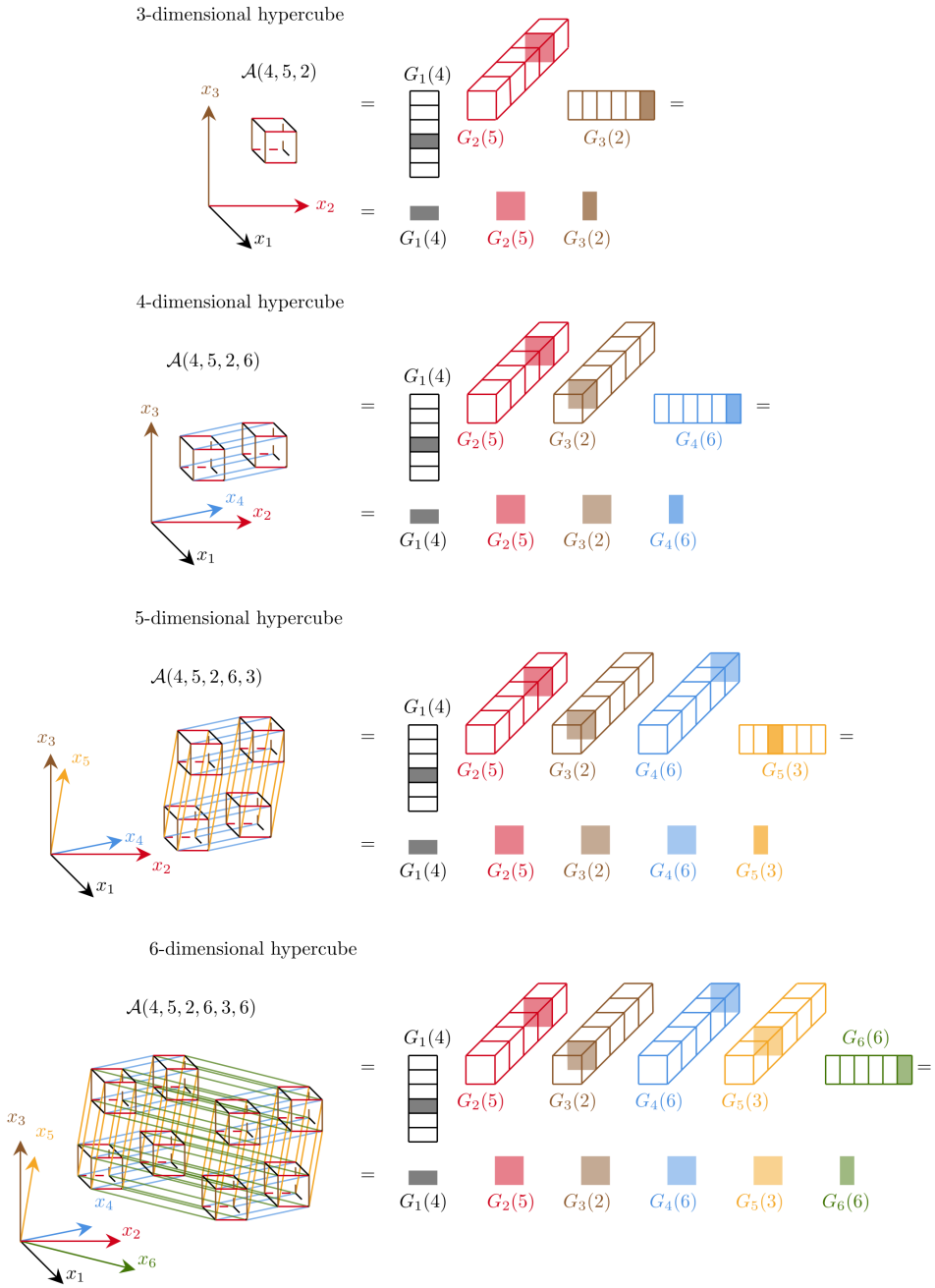

Figure 11: In this picture we present the progression from a three to a six dimensional array in full and Tensor Train format.

a similar *TT format for linear operators*, i.e., "*multi-dimensional matrices*" $\mathcal{L}(i,j)$ that depend on two d-dimensional multi-indices $i = (i_1, i_2, \ldots, i_d)$ and $j = (j_1, j_2, \ldots, j_d)$. The formal definition reads as

$$\mathcal{L}\Big(\big(i_1, i_2, \ldots, i_d\big), \big(j_1, j_2, \ldots, j_d\big)\Big) = \mathcal{L}\Big(\big(i_1, j_1\big), \big(i_2, j_2\big), \ldots, \big(i_d, j_d\big)\Big)$$

$$= \sum_{\alpha_1=1}^{r_1} \sum_{\alpha_2=1}^{r_2} \ldots \sum_{\alpha_{d-1}=1}^{r_{d-1}} L_1\big(1, (i_1, j_1), \alpha_1\big)\, L_2\big(\alpha_2, (i_2, j_2), \alpha_3\big) \ldots L_d\big(\alpha_{d-1}, (i_d, j_d), 1\big), \quad (10)$$

where the first equality follows from a convenient index permutation to form the index pairs (i_ℓ, j_ℓ), $\ell = 1, 2, \ldots, d$.

The so-called "*core notation*" gives a more intuitive insight into the structure of the cores:

$$A_\ell = \begin{bmatrix} A_\ell(1,:,1) & A_\ell(1,:,2) & \dots & A_\ell(1,:,r_\ell) \\ A_\ell(2,:,1) & A_\ell(2,:,2) & \dots & A_\ell(2,:,r_\ell) \\ \vdots & \vdots & \vdots & \vdots \\ A_\ell(r_{\ell-1},:,1) & A_\ell(r_{\ell-1},:,2) & \dots & A_\ell(r_{\ell-1},:,r_\ell) \end{bmatrix},$$

$$L_\ell = \begin{bmatrix} L_\ell(1,:,:,1) & L_\ell(1,:,:,2) & \dots & L_\ell(1,:,:,r_\ell) \\ L_\ell(2,:,:,1) & L_\ell(2,:,:,2) & \dots & L_\ell(2,:,:,r_\ell) \\ \vdots & \vdots & \vdots & \vdots \\ L_\ell(r_{\ell-1},:,:,1) & L_\ell(r_{\ell-1},:,:,2) & \dots & L_\ell(r_{\ell-1},:,:,r_\ell) \end{bmatrix}.$$

With such notation and using the definition of the strong Kroncker product [9] "$\bowtie$", we write the TT decomposition in the more compact form:

$$\mathcal{A} = A_1 \bowtie A_2 \bowtie \dots \bowtie A_d, \qquad \mathcal{L} = L_1 \bowtie L_2 \bowtie \dots \bowtie L_d.$$

We will make use of this mathematical formalism to describe the different parts of $\mathrm{T}^2\mathrm{S}^2$.

Tensor-train (TT) decomposition The construction of an optimal tensor-train representation for a d-dimensional tensor can be achieved through the TT-SVD algorithm [40]. This algorithm builds the TT decomposition through a systematic application of singular value decompositions on specific matrix representations of the tensor, known as *unfoldings*. For a d-dimensional tensor $\mathcal{A}$, we consider $d-1$ "fundamental" matrix unfoldings. The ℓ-th unfolding, denoted as A_ℓ, reorganizes the tensor entries into a matrix of size $(\prod_{k=1}^{\ell} n_k) \times (\prod_{k=\ell+1}^{d} n_k)$ through the relation:

$$A_\ell(\eta_\ell(i_1,\dots,i_\ell), \eta'_\ell(i_{\ell+1},\dots,i_d)) = \mathcal{A}(i_1,\dots,i_d), \tag{11}$$

where η_ℓ and η'_ℓ are two bijective mappings between the respective index tuples, e.g., $(i_1,\dots,i_\ell)$ and $(i_{\ell+1},\dots,i_d)$, often called "long indices", and the row and column indices of matrix A_ℓ. A very strong connection exists between the TT-ranks of tensor $\mathcal{A}$ and the ranks of the unfolding matrices. In fact, the rank of the ℓ-th matrix unfolding is a lower bound for the TT-rank r_ℓ, and a constructive proof shows that TT-SVD can compute an *exact* TT-representation with TT-ranks r_ℓ equal to the ranks of the matrix unfoldings A_ℓ [40, Theorem 2.1], i.e., $r_\ell = \mathrm{rank}(A_\ell)$ for $\ell = 1,\dots,d-1$.

Of particular practical importance is the existence of low-rank approximations. The sequential nature of the TT-SVD algorithm ensures that the TT ranks are optimal in the sense that they provide the best possible approximation for a given accuracy threshold. If we truncate the singular values in the TT-SVD algorithm below a give threshold ϵ, the resulting approximation error in the Frobenius norm is bounded by $\epsilon\sqrt{d-1}\|\mathcal{A}\|_F$. Such an approximate TT decomposition keeps the TT ranks minimal while achieving the accuracy prescribed by ϵ. Therefore, when computational constraints or data compression requirements need smaller ranks $r'_\ell \leq \mathrm{rank}(A_\ell)$, a best approximation $\mathcal{A}^{TT}_{\text{best}}$ in the tensor-train format is guaranteed to exist.

The TT-SVD algorithm efficiently provides a quasi-optimal approximation $\mathcal{A}^{TT}$ in the sense that:

$$\|\mathcal{A} - \mathcal{A}^{TT}\|_{\mathcal{F}} \leq \sqrt{d-1} \inf_{\mathcal{B}^{TT} \in \mathbb{TT}(\mathbf{r}'_\ell)} \|\mathcal{A} - \mathcal{B}^{TT}\|_{\mathcal{F}}. \tag{12}$$

Here, $\mathbb{TT}(\mathbf{r}'_\ell)$ denotes the manifold of tensor-train representations with prescribed rank $\mathbf{r}'_\ell = (r'_1,\dots,r'_{d-1})$, and the multiplicative factor $\sqrt{d-1}$ represents the stability constant of the algorithm [39]. This quasi-optimality result establishes TT-SVD as a practical tool for tensor approximation, offering a controlled trade-off between computational efficiency and approximation accuracy.

The tensor-train format supports the efficient implementation of fundamental multi-linear algebraic operations such as scalar multiplication, tensor addition, element-wise (Hadamard) products, and contractions with matrices and vectors [40]. These operations are designed to preserve the tensor-train structure but they generally lead to an increase in the TT ranks of the resulting tensor. A critical step is the so-called rounding procedure, denoted as $\mathsf{rndg}(\,\cdot\,)$, which "recompresses" the tensor by computing a new TT representation with smaller ranks while controlling the approximation error [40]. Given a tensor $\mathcal{A}$ in TT-format, the "rounded" tensor $\mathsf{rndg}(\mathcal{A})$ satisfies the inequality $\|\mathcal{A} - \mathsf{rndg}(\mathcal{A})\|_{\mathcal{F}} \leq \epsilon\|\mathcal{A}\|_{\mathcal{F}}$, where ϵ is a threshold parameter that makes a trade-off between accuracy and computational costs possible. On the one hand, smaller values of ϵ can preserve a better accuracy but implies higher TT ranks, hence

increasing the computational costs and storage requirements. On the other hand, larger values of ϵ lead to a better compression with lower ranks, thus reducing computational complexity at the expense of accuracy. This balance between accuracy and efficiency must be carefully calibrated according to the specific requirements of the application at hand.

Finally, it is worth mentioning the cross-approximation technique [39], which allows us to compute the TT representation of a tensor by sampling only a small subset of its entries. This algorithm makes the calculation of a TT decomposition very efficient since in many applications, mainly when dealing with function-generated tensors, computing and storing the full tensor is prohibitively expensive or impossible. Cross-interpolation typically employs the MaxVol algorithm[24], a sophisticated sampling strategy that selectively chooses optimal rows and columns from the tensor to construct its TT representation. In our context, cross-interpolation proves particularly valuable for efficiently representing the right-hand side term f, allowing us to work with high-dimensional data while maintaining computational tractability.

References

[1] *Advanced Reactor Information System.* URL :https://aris.iaea.org/ (Last accessed February 9th, 2025). 2025.

[2] D. N. Arnold. *Numerical Analysis of Partial Differential Equations.* Lecture Notes. Lecture notes for Math 8445-8446, Last modified March 22, 2018. University of Minnesota, 2018. URL: https://www-users.cse.umn.edu/~arnold/8445-8446.17-18/notes.pdf (visited on 09/25/2024).

[3] G. I. Bell and S. Glasstone. *Nuclear Reactor Theory.* English. (TID-25606, osti_id 4074688, NSA-25-010317). US Atomic Energy Commission, Washington, DC (United States): US Atomic Energy Commission (AEC), 1970. URL: https://www.osti.gov/biblio/4074688.

[4] R. Bellman. *Dynamic Programming.* Princeton, NJ: Princeton University Press, 1957.

[5] A. N. Brooks and T. J. R. Hughes. "Streamline upwind/Petrov-Galerkin formulations for convection dominated flows with particular emphasis on the incompressible Navier-Stokes equations". In: *Computer Methods in Applied Mechanics and Engineering* 32.1 (1982), pp. 199–259. ISSN: 0045-7825. DOI: https://doi.org/10.1016/0045-7825(82)90071-8. URL: https://www.sciencedirect.com/science/article/pii/0045782582900718.

[6] C. Canuto et al. *Spectral Methods: Fundamentals in Single Domains.* Springer Berlin Heidelberg, 2007. ISBN: 9783540307266. URL: https://books.google.it/books?id=DFJB0kiq0CQC.

[7] N. Cavallini et al. "Vanquishing the computational cost of passive gamma emission tomography simulations leveraging physics-aware reduced order modeling". In: *Scientific Reports* 13 (2023), p. 15034. DOI: 10.1038/s41598-023-41220-3.

[8] C. Cercignani. *The Boltzmann Equation and Its Applications.* Applied Mathematical Sciences. Springer New York, 2012. ISBN: 9781461210399. URL: https://books.google.it/books?id=OcTcBwAAQBAJ.

[9] W. De Launey and J. Seberry. "The strong Kronecker product". In: *Journal of Combinatorial Theory, Series A* 66.2 (1994), pp. 192–213. ISSN: 0097-3165. DOI: https://doi.org/10.1016/0097-3165(94)90062-0.

[10] F. De l'Isle and R. G. Owens. "A superconsistent collocation method for high Reynolds number flows". In: *Computers & Fluids* 259 (2023), p. 105897. ISSN: 0045-7930. DOI: https://doi.org/10.1016/j.compfluid.2023.105897.

[11] F. De l'Isle and R. G. Owens. "Superconsistent collocation methods with applications to convection-dominated convection–diffusion equations". In: *Journal of Computational and Applied Mathematics* 391 (2021), p. 113367. ISSN: 0377-0427. DOI: https://doi.org/10.1016/j.cam.2020.113367. URL: https://www.sciencedirect.com/science/article/pii/S0377042720306580.

[12] S. V. Dolgov, B. N. Khoromskij, and I. V. Oseledets. "Fast Solution of Parabolic Problems in the Tensor Train/Quantized Tensor Train Format with Initial Application to the Fokker–Planck Equation". In: *SIAM Journal on Scientific Computing* 34.6 (2012), A3016–A3038. DOI: 10.1137/120864210. eprint: https://doi.org/10.1137/120864210. URL: https://doi.org/10.1137/120864210.

[13] S. V. Dolgov and D. V. Savostyanov. "Alternating Minimal Energy Methods for Linear Systems in Higher Dimensions". In: *SIAM Journal on Scientific Computing* 36.5 (2014), A2248–A2271. DOI: 10.1137/140953289. URL: https://doi.org/10.1137/140953289.

[14] S. V. Dolgov and D. V. Savostyanov. "Alternating minimal energy methods for linear systems in higher dimensions. Part II: Faster algorithm and application to nonsymmetric systems". In: *SIAM, Journal on Scientific Computing* 37.5 (2015), A2456–A2488. DOI: https://doi.org/10.1137/140953289.

[15] S. V. Dolgov and R. Scheichl. "A Hybrid Alternating Least Squares–TT Cross Algorithm for Parametric PDEs". In: *SIAM/ASA Journal on Uncertainty Quantification* 7.1 (2019), pp. 260–291. DOI: 10.1137/18M1194134.

[16] L. Einkemmer and A. Moriggl. "Semi-Lagrangian 4d, 5d, and 6d kinetic plasma simulation on large-scale GPU-equipped supercomputers". In: *The International Journal of High Performance Computing Applications* 37.2 (2023), pp. 180–196. DOI: 10.1177/10943420221137599.

[17] L. Einkemmer et al. *A review of low-rank methods for time-dependent kinetic simulations*. arXiv:2412.05912. 2024. eprint: 2412.05912 (math.NA). URL: https://arxiv.org/abs/2412.05912.

[18] J. Fish and T. Belytschko. *A first course in finite elements*. Wiley, 2007.

[19] D. Funaro. *Spectral Elements for Transport-Dominated Equations*. Springer Berlin Heidelberg, 1997. ISBN: 9783540626497. URL: https://books.google.it/books?id=vieH0KmZ-n4C.

[20] D. Funaro. "Superconsistent Discretizations". In: *Journal of Scientific Computing* 17.1 (2002), pp. 67–79. DOI: 10.1023/A:1015136227726. URL: https://doi.org/10.1023/A:1015136227726.

[21] W. H. Geist, P. A. Santi, and M. T. Swinhoe, eds. *Nondestructive Assay of Nuclear Materials for Safeguards and Security*. Cham: Springer, 2024. DOI: 10.1007/978-3-031-58277-6.

[22] R. Glowinski. "Finite element methods for incompressible viscous flow". In: *Numerical Methods for Fluids (Part 3)*. Vol. 9. Handbook of Numerical Analysis. Elsevier, 2003, pp. 3–1176. DOI: https://doi.org/10.1016/S1570-8659(03)09003-3. URL: https://www.sciencedirect.com/science/article/pii/S1570865903090033.

[23] R. Glowinski and T. W. Pan. *Numerical Simulation of Incompressible Viscous Flow*. De Gruyter, 2022. ISBN: 9783110785012. URL: https://doi.org/10.1515/9783110785012.

[24] S. Goreinov et al. "How to Find a Good Submatrix". In: *Matrix Methods: Theory, Algorithms and Applications*. Ed. by V. Olshevsky and E. Tyrtyshnikov. Singapore: World Scientific, 2010. Chap. 15, pp. 247–256. DOI: 10.1142/9789812836021_0015.

[25] F. Graziani, ed. *Computational Methods in Transport*. Springer-Verlag Berlin Heidelberg, 2006. DOI: 10.1007/3-540-28125-8. URL: https://doi.org/10.1007/3-540-28125-8.

[26] F. R. Graziani and G. L. Olson. *Transport Methods Conquering the seven-dimensional Mountain*. Tech. rep. UCRL-JC-154432. Lawrence Livermore National Laboratory, 2003.

[27] J. S. Hesthaven, S. Gottlieb, and D. Gottlieb. *Spectral Methods for Time-Dependent Problems*. Vol. 21. Cambridge Monographs on Applied and Computational Mathematics. Cambridge University Press, 2007.

[28] J. S. Hesthaven, G. Rozza, and B. Stamm. *Certified Reduced Basis Methods for Parametrized Partial Differential Equations*. 1st ed. Springer Briefs in Mathematics. Switzerland: Springer, 2015, p. 135.

[29] T. J. R. Hughes and M. Mallet. "A new finite element formulation for computational fluid dynamics: III. The generalized streamline operator for multidimensional advective-diffusive systems". In: *Computer Methods in Applied Mechanics and Engineering* 58.3 (1986), pp. 305–328. ISSN: 0045-7825. DOI: https://doi.org/10.1016/0045-7825(86)90152-0. URL: https://www.sciencedirect.com/science/article/pii/0045782586901520.

[30] W. Hundsdorfer and J. G.a Verwer. *Numerical Solution of Time-Dependent Advection-Diffusion-Reaction Equations*. Vol. 33. Springer-Verlag, 2003. DOI: 10.1007/978-3-662-09017-6.

[31] *IAEA World Fusion Outlook 2024*. URL https://www.iaea.org/publications/15777/iaea-world-fusion-outlook-2024 (last accessed February 21st, 2025). Vienna, 2024.

[32] A. Jüngel. *Transport Equations for Semiconductors*. Lecture Notes in Physics. Springer, 2009. ISBN: 9783540895251. URL: https://books.google.it/books?id=d6YIyevAQG4C.

[33] T. Kolda and B. Bader. "Tensor decompositions and applications". In: *SIAM Review* 51.3 (2009), pp. 455–500.

[34] Katharina Kormann. "A Semi-Lagrangian Vlasov Solver in Tensor Train Format". In: *SIAM Journal on Scientific Computing* 37.4 (2015), B613–B632. DOI: 10.1137/140971270. eprint: https://doi.org/10.1137/140971270. URL: https://doi.org/10.1137/140971270.

[35] J. N. Kutz. *Data-Driven Modeling & Scientific Computation: Methods for Complex Systems & Big Data*. USA: Oxford University Press, Inc., 2013. ISBN: 0199660344.

[36] J. N. Kutz et al. *Dynamic Mode Decomposition*. Philadelphia, PA: Society for Industrial and Applied Mathematics, 2016. DOI: 10.1137/1.9781611974508. eprint: https://epubs.siam.org/doi/pdf/10.1137/1.9781611974508. URL: https://epubs.siam.org/doi/abs/10.1137/1.9781611974508.

[37] N. Malaya et al. "MASA: A library for verification using manufactured and analytical solutions". In: *Engineering with Computers* (2012), pp. 1–10. ISSN: 0177-0667. DOI: 10.1007/s00366-012-0267-9.

[38] H. Meuer et al. *TOP500*. (online article). 2025. URL: https://top500.org (visited on 02/18/2025).

[39] I. Oseledets and E. Tyrtyshnikov. "TT-cross approximation for multidimensional arrays". In: *Linear Algebra and its Applications* 432.1 (2010), pp. 70–88.

[40] I. V. Oseledets. "Tensor-Train Decomposition". In: *SIAM Journal on Scientific Computing* 33.5 (2011), pp. 2295–2317. DOI: 10.1137/090752286. URL: https://doi.org/10.1137/090752286.

[41] *Reports - Exascale Computing Project*. URL: https://www.exascaleproject.org/reports/ (Last accessed February 9th, 2025). 2025.

[42] L. Ruthotto et al. "A machine learning framework for solving high-dimensional mean field game and mean field control problems". In: *Proceedings of the National Academy of Sciences* 117.17 (2020), pp. 9183–9193. DOI: 10.1073/pnas.1922204117.

[43] S. J. Ruuth and R. J. Spiteri. "A new class of optimal high-order strong-stability-preserving time discretization methods". In: *SIAM J. Numer. Anal* 40 (2003), pp. 469–491.

[44] W. E. Schiesser. *The Numerical Method of Lines: Integration of Partial Differential Equations*. Academic Press, 1991. ISBN: 978-0126241303.

[45] H. Smith and H. H. Jensen. *Transport Phenomena*. Clarendon Press, 1989. ISBN: 9780198519850. URL: https://books.google.it/books?id=xPt9AAAAIAAJ.

[46] Hillel Tal-Ezer. "Spectral methods in time for hyperbolic equations". In: *SIAM Journal on Numerical Analysis* 23.1 (1986), pp. 11–26.

[47] B. R. Wienke. "Transport equations in moving material. Part I: Neutrons and photons". In: *Progress in Nuclear Energy* 46.1 (2005), pp. 13–55. ISSN: 0149-1970. DOI: https://doi.org/10.1016/j.pnucene.2004.09.016. URL: https://www.sciencedirect.com/science/article/pii/S0149197004000770.

[48] M. M. R. Williams. *Random Processes in Nuclear Reactors*. Pergamon, 2013. ISBN: 9781483187273. URL: https://books.google.it/books?id=FkP-BAAAQBAJ.

[49] G. P. Zank. *Transport Processes in Space Physics and Astrophysics*. 2014th ed. Springer New York, 2014. URL: https://doi.org/10.1007/978-1-4614-8480-6.

[50] J. Zhou, R. Li, and T. Luo. "Physics-informed neural networks for solving time-dependent mode-resolved phonon Boltzmann transport equation". In: *npj Computational Materials* 9.1 (2023), p. 212. DOI: 10.1038/s41524-023-01165-7.